ADVANCING EARTH AND SPACE SCIENCES

JGR Space Physics

RESEARCH ARTICLE

10.1029/2025JA033871

Modeling the Internal Redistribution of Earth's Proton Radiation Belt by Interplanetary Shocks

Alexander R. Lozinski[1], Adam C. Kellerman[1], Jacob Bortnik[1], Richard B. Horne[2], Ravindra T. Desai[2,3,4], and Sarah A. Glauert[2]

[1]Department of Atmospheric and Oceanic Sciences, UCLA, Los Angeles, CA, USA, [2]British Antarctic Survey, Cambridge, UK, [3]Centre for Fusion, Space & Astrophysics, University of Warwick, Coventry, UK, [4]Blackett Laboratory, Imperial College London, London, UK

Key Points:

- The 24 March 1991 interplanetary shock produced an enhancement of 1–20 MeV proton flux at $L = 2$ by up to one order of magnitude
- The shock-induced electric field pulse interacted resonantly with $M \approx 400$ MeV/G radiation belt protons to transport them toward this region
- We demonstrate a new method to predict changes in phase space density due to shock redistribution, producing good agreement with CRRES data

Correspondence to:

A. R. Lozinski,
alozinski@atmos.ucla.edu

Citation:

Lozinski, A. R., Kellerman, A. C., Bortnik, J., Horne, R. B., Desai, R. T., & Glauert, S. A. (2025). Modeling the internal redistribution of Earth's proton radiation belt by interplanetary shocks. *Journal of Geophysical Research: Space Physics*, *130*, e2025JA033871. https://doi.org/10.1029/2025JA033871

Received 21 FEB 2025
Accepted 10 JUN 2025

Abstract A large proton belt enhancement occurred on 24 March 1991 following an interplanetary shock that impacted the dayside magnetopause at ~03:40 UT. Its formation was measured by the proton telescope aboard CRRES and attributed to the injection and inward transport of solar energetic particles (SEPs) by an azimuthally propagating electric field pulse induced by the shock's compression of the magnetosphere. This led to an increase in the flux of high energy (>25 MeV) protons by several orders of magnitude at $L \approx 2.5$ which has been well-studied. However, a flux enhancement by up to one order of magnitude was also seen in 1–20 MeV protons at $L \approx 2$. Protons in this energy range pose a hazard to orbiting spacecraft as a major contributor to solar cell nonionizing dose. The 1–20 MeV enhancement cannot be explained by the inward transport of a solar proton source, because a newly injected source population at the required energy would have a drift velocity too low to interact with the pulse. Instead, we hypothesize that the 1–20 MeV enhancement was caused by the redistribution of radiation belt protons to different drift shells by the pulse. To test this hypothesis, we apply a novel method to predict the change in phase space density during a shock event which utilizes reverse-time particle tracing simulations. Our results show that the 1–20 MeV enhancement can be accounted for by internal redistribution as hypothesized. We thus identify a new mechanism for proton belt enhancements that does not depend on a SEP source and present a way to model it.

1. Introduction

The proton radiation belt consists of protons ranging from hundreds of kiloelectron volts (keV) up to hundreds of megaelectron volts (MeV) exhibiting adiabatic motion under the influence of Earth's geomagnetic field. Their trajectories are confined to drift shells surrounding Earth, and described by a set of three adiabatically invariant parameters M, α_{eq} and L, where M is the magnetic moment, α_{eq} is equatorial pitch angle, and L refers to the McIlwain L shell. During geomagnetically quiet periods, the proton belt occupies up to $L \sim 3$ at ~20 MeV (Selesnick & Looper, 2023). At energies of hundreds of keV and below, the orbits of trapped protons can extend to $7 \lesssim L \lesssim 9$, with the region $L \gtrsim 4$ known as the ring current (Daglis et al., 1999; Sergeev & Tsyganenko, 1982; Williams, 1987).

A radiation belt proton is considered trapped when magnetic field strength is sufficient to preserve its three invariants over multiple drift orbits. Protons produced via cosmic ray albedo neutron decay (CRAND) are the primary source of the distribution observed at $\gtrsim$50 MeV and $L \lesssim 1.5$ (X. Li et al., 2017; Selesnick et al., 2007; S. F. Singer, 1958), and can be trapped instantaneously. Protons of solar origin also provide a source. Kress et al. (2021, Figure 4) present an example of their arrival at geostationary altitude as shown by Geostationary Operational Environmental Satellite (GOES) measurements of proton flux over 4–10 September 2017. In this case, flux intensified in time with the arrival of two interplanetary shocks on 7 and 8 September due to "energetic storm particles," which undergo local acceleration at interplanetary shock fronts (Mäkelä et al., 2011). Other intensifications can also be seen before and after shock arrival. These were due to solar energetic particles (SEPs), which are accelerated ahead of shocks in interplanetary space and may thus arrive separately to a shock (Reames, 2001).

The trajectories of incoming solar protons are attenuated by the magnetosphere. The accessible region within a given field configuration is determined by the particle's magnetic rigidity and defined by a geomagnetic cutoff rigidity surface (Kress et al., 2004). Using test particle simulations, Kress et al. (2005) showed that shock-driven compression of the magnetosphere can suppress cutoff surfaces such that 25 MeV SEP protons are temporarily allowed access to $L \sim 3.5$. Furthermore, the authors demonstrated that SEPs can become trapped in an inner access region if the field reverts within a drift period.

The GOES P1 channel (1–1.9 MeV) nominally measures trapped protons (Figure 2, Kress et al., 2021). The intensification in flux by several orders of magnitude that is recorded during shock arrival is therefore evidence of cutoff suppression, and shows that $\sim$1 MeV solar protons can access geostationary altitude. At higher energy, cutoff occurs at lower altitude: Z. Li et al. (2021) present measurements from the NASA Van Allen Probes over the 7–8 September 2017 period which show the trapping of 21.1 MeV protons at $L \sim 3$ coinciding with the aforementioned shocks, supporting the results of Kress et al. (2005). However, protons with $E \gtrsim 10$ MeV in this region are subject to field line curvature scattering loss on small timescales (Lozinski et al., 2024; Selesnick & Looper, 2023), and as a result the 7–8 September enhancement decayed over approximately one day.

A significantly larger enhancement of the proton belt was measured by the proton telescope (PROTEL) instrument aboard CRRES following an interplanetary shock that arrived at the magnetopause boundary at ~03:40 UT, 24 March 1991 (Blake et al., 1992; Violet et al., 1993). This enhancement was characterized by an increase in ~50 MeV flux by more than two orders of magnitude at $L = 2.5$, and persisted for several months until the end of the mission (Plate 1 of Albert et al., 1998). The depth of particle injection was attributed to an azimuthally propagating electric field pulse induced by the shock's compression of the magnetosphere (Hudson et al., 1997; X. Li et al., 1993). An SEP source first accessed the magnetosphere, and those particles drifting in phase with the pulse were then coherently accelerated inward, reaching down to $L \sim 2.5$ (Hudson et al., 1996). This occurred on a timescale comparable to one drift orbit, thus conserving M.

The formation of this enhancement at $\gtrsim$20 MeV has been well-studied in literature. However, PROTEL measurements following the 24 March 1991 event also showed an enhancement in the flux of equatorially mirroring $\sim$5 MeV protons at $L \approx 2$ (Figure 4, Lozinski, Horne, Glauert, Del Zanna, & Albert, 2021). This corresponds to $M \approx 130$ MeV/G, which is equivalent in a dipole to $E \approx 0.65$ MeV, $v_d \approx 160$km/s at $L = 4$, or $E \approx 0.21$ MeV, $v_d \approx 120$ km/s at $L = 6$. This means that the $\sim$5 MeV enhancement cannot be explained by the prompt injection and inward transport of a solar proton source because a newly injected source population with comparable M would have a drift velocity around one tenth that of the pulse propagation speed ($\sim$2000 km/s, X. Li et al., 1993), and therefore would not achieve drift-resonance with the pulse as required for inward transport to such low L (Hudson et al., 2023). Some other mechanism is thus required to explain the enhancement of protons at ~MeV energies.

In addition to the 24 March 1991 event, recent measurements by various satellites following the 10 May 2024 superstorm show an enhancement in ~MeV flux at $L \sim 2$, highlighting the need for better understanding of the underlying mechanism (Pierrard et al., 2024). Enhancements such as these are of particular importance to the satellite industry, because 1–20 MeV protons are responsible for damaging radiation effects (i.e., Miyake et al., 2014; Jenkins et al., 2014; Rodbell, 2020), and because of the increasing utilization of LEO and MEO orbits, which are particularly exposed to fluxes of MeV protons (Horne & Pitchford, 2015; Lozinski et al., 2019).

In this study, we analyze the enhancement of 1–20 MeV proton flux measured by CRRES following the March 1991 event, and hypothesize that it was caused by the internal, nonadiabatic redistribution of radiation belt protons to different drift orbits by the electric field pulse, which was driven by the shock. To test this hypothesis, we develop a novel method to predict the change in phase space density as a result of particle redistribution during a shock event. This method requires as input: (a) the pre-storm distribution of phase space density; (b) a model of the disturbance electromagnetic field, which we take from X. Li et al. (1993); and (c) a reverse-time simulation of test particles using the newly developed Trajectory Redistribution In Phase Space (TRIPS) code. Section 2 details the pre-storm distribution and model field pulse, Section 3 explains the method, and Section 4 presents predictions of 1–20 MeV proton phase space density from $L = 1.8$ to 2.1 in the post-March 1991 event period. Our results show that the enhancement in 1–20 MeV phase space density observed by CRRES can be accounted for by the internal redistribution of a pre-existing trapped population of protons. We thus draw attention to an important mechanism that leads to proton belt enhancements, and present a way to model future enhancements at this crucial energy range.

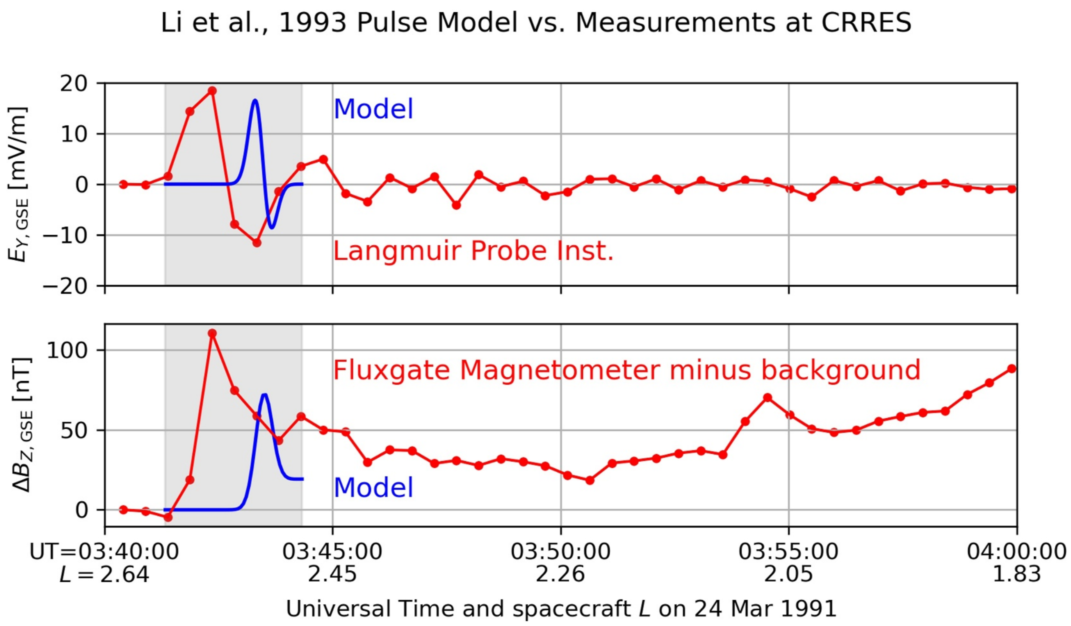

Figure 1. Measured and modeled fields on 24 March 1991. Top panel: electric field Y-component in the GSE frame, model of X. Li et al. (1993, blue) versus data (red). Bottom panel: offset magnetic field Z-component in the GSE frame induced by the electric field, model (blue) versus data (red). To produce the magnetic field data, the T89 external field was subtracted from measurements, then a bias was added such that $\Delta B_{Z,GSE} = 0$ at the earliest time shown.

2. The 24 March 1991 Event

2.1. Modeling the Electromagnetic Field

On 24 March 1991 a large interplanetary shock impacted Earth's magnetosphere at ~03:40 UT, coincident with the arrival of SEPs. The rapid compression and subsequent relaxation of the magnetosphere caused by the shock induced an azimuthally propagating electric field pulse with a bipolar signature, which accelerated a portion of the arriving SEPs down to $L \sim 2.5$ (Violet et al., 1993; Blake et al., 1992; X. Li et al., 1993; Hudson et al., 1997). The event was observed in real-time by the CRRES satellite, which collected measurements of the initial electric field pulse using the onboard Langmuir Probe instrument, as well as measurements of proton radiation belt flux over the ensuing ~6 months using the onboard PROTEL instrument.

X. Li et al. (1993) developed the following empirical model to describe the azimuthally propagating electric field component throughout the magnetosphere:

$$\boldsymbol{E_w} = -\hat{e}_{\bar{\phi}} E_0 \left(1 + c_1 \cos\left(\bar{\phi} - \overline{\phi_0}\right)\right) \left[\exp\left(-\xi^2 - c_2 \exp\left(-\eta^2\right)\right)\right] \tag{1}$$

where $\xi = [r + v_0(t - t_{ph})]$, $\eta = [r - v_0(t - t_{ph} + t_d)]$, $t_{ph} = t_i + (c_3 R_E / v_0)\left[1 - \cos\left(\bar{\phi} - \bar{\phi}_0\right)\right]$, $E_0 = 240$ mV/m, $v_0 = 2000$ km/s, $c_1 = 0.8$, $c_2 = 0.8$, $c_3 = 8.0$, $t_i = 80$ s, $t_d = 2.06 R_E / v_0$, $\bar{\phi}_0 = 45°$, $d = 30000$ km, and $\left(r, \theta, \bar{\phi}\right)$ is a set of spherical coordinates in the geocentric solar ecliptic (GSE) frame. A description of each parameter is given in X. Li et al. (1993).

We modeled the time-varying electromagnetic field associated with this event using Equation 1 for the electric field, then solving for the associated magnetic field perturbation $\boldsymbol{B_w}$ by applying Faraday's law, as also demonstrated in X. Li et al. (1993). The background magnetic field was modeled using a dipole with equatorial surface field strength $B_0 = 3.0293 \times 10^{-5}$ T. The combined electromagnetic field was then stored on a grid of cartesian spatial coordinates in the geomagnetic coordinate system (MAG) at a resolution of $\Delta X \approx 0.16 R_E$ and $\Delta t \approx 3.7$ s for use in particle tracing simulations.

Figure 1 compares the electric and magnetic field perturbations modeled using Equation 1 and interpolated to CRRES' location (blue), to measurements taken by CRRES (red) over the course of the event, with the modeling period for this study highlighted in gray. Measurements in the top panel of Figure 1 are from the CRRES Langmuir Probe, and show the electric field Y-component in the GSE reference frame at the native 30s resolution of the data set (Mozer & Mullen, 2025). Measurements in the bottom panel show an offset magnetic field Z-component in the GSE frame as an approximation of the perturbation induced by the electric field, derived by subtracting a background magnetic field from measurements taken by the CRRES Fluxgate Magnetometer instrument (H. J. Singer & Mullen, 2010).

Whilst deriving the offset magnetic field Z-component in Figure 1 (bottom panel), it was found that the offset could be biased up or down by hundreds of nanotesla depending on the choice of magnetic field model used to calculate the background, hindering model comparison. Therefore, after subtracting the background field, we took the extra step of applying a bias such that $\Delta B_{Z,GSE} = 0$ at the earliest epoch shown (03:40:00 UT). The T89 field model (Tsyganenko, 1989) was chosen to calculate the background because it resulted in an offset similar to that shown in X. Li et al. (1993). As a result of this process, variation over the simulation period is highlighted. The blue line shows the model magnetic field perturbation Z-component obtained from Faraday's law and loaded from the numerical grid for comparison.

Figure 1 highlights both a phase and amplitude difference between the model and data in both the electric and magnetic perturbations at CRRES' location. These are in line with those demonstrated by Figure 1 of X. Li et al. (1993), which differs slightly by plotting the reversed azimuthal component of the simulation electric field. The disagreement between model and data represents the limitation posed by the eight free parameters of Equation 1, which are estimated such that the model captures overall time evolution across the entire magnetosphere.

2.2. Measurements From PROTEL

The Proton Telescope (PROTEL) instrument on-board the CRRES satellite made measurements of differential flux on 24 energy channels in the 1–100 MeV range with full pitch angle resolution (Violet et al., 1993). Measurements were made from elliptical orbit (350 km perigee, 36,000 km apogee) at 18° inclination. PROTEL data for the present study was extracted from the PROTEL ".min" files (Mullen & Brautigam, 2021). These files contain data from 15 August 1990 until 11 October 1991, with one minute-averaged flux available in 5° bins in local pitch angle, ranging from 0 to 90° for 18 bins in total. The data processing methodology used in this study is the same as applied in Lozinski, Horne, Glauert, Del Zanna, and Albert (2021), which contains a full description of caveats.

Issues encountered whilst processing the PROTEL data included measurement noise within each pitch angle bin and a shortage of measurements at $\alpha_{\mathrm{eq}} \gtrsim 85°$ surrounding the 24 March 1991 study period. To address this, measurements were averaged over 1-week time windows throughout the CRRES period, resulting in flux for each average period, pitch angle bin and energy channel. These datapoints were then fit using the model

$$j = A \sin^{n}(\alpha_{\mathrm{eq}}) \tag{2}$$

where j is differential, unidirectional flux, α_{eq} is equatorial pitch angle, and A, n are fitting parameters. A standard deviation was also calculated for each datapoint from the measurements of flux within each average period. In general, j given by Equation 2 was found to be well within one standard deviation of the data, providing a close fit. One disadvantage of Equation 2 is that it is prone to over-predict flux at $\alpha_{\mathrm{eq}} \approx 90°$ when the distribution is highly anisotropic ($n > 20$), but this did not contribute significant error to our study.

An overview of the PROTEL data throughout the region of interest to this study is presented in Figure 2, showing average differential flux through time at $\alpha_{\mathrm{eq}} = 90°$ (left panels), along with anisotropy $\log_{10}(n)$ of pitch angle distributions (right panels) in L bins from 1.4 to 2.5. Both quantities were derived from the fits given by Equation 2, in which small values of n correspond to a more isotropic distribution whilst large values of n correspond to an anisotropic distribution strongly peaked at $\alpha_{\mathrm{eq}} = 90°$. Vertical black lines in Figure 2 indicate magnetic disturbances that occurred during the CRRES mission corresponding to Table 1 of Hudson et al. (1997), with the fourth from left corresponding to the 24 March 1991 event.

Figure 2 demonstrates the dramatic enhancements in flux following the 24 March 1991 event. At ~50 MeV, the top left panel shows the creation of a new proton belt at $L \gtrsim 2$. The lower panels show an enhancement by up to an

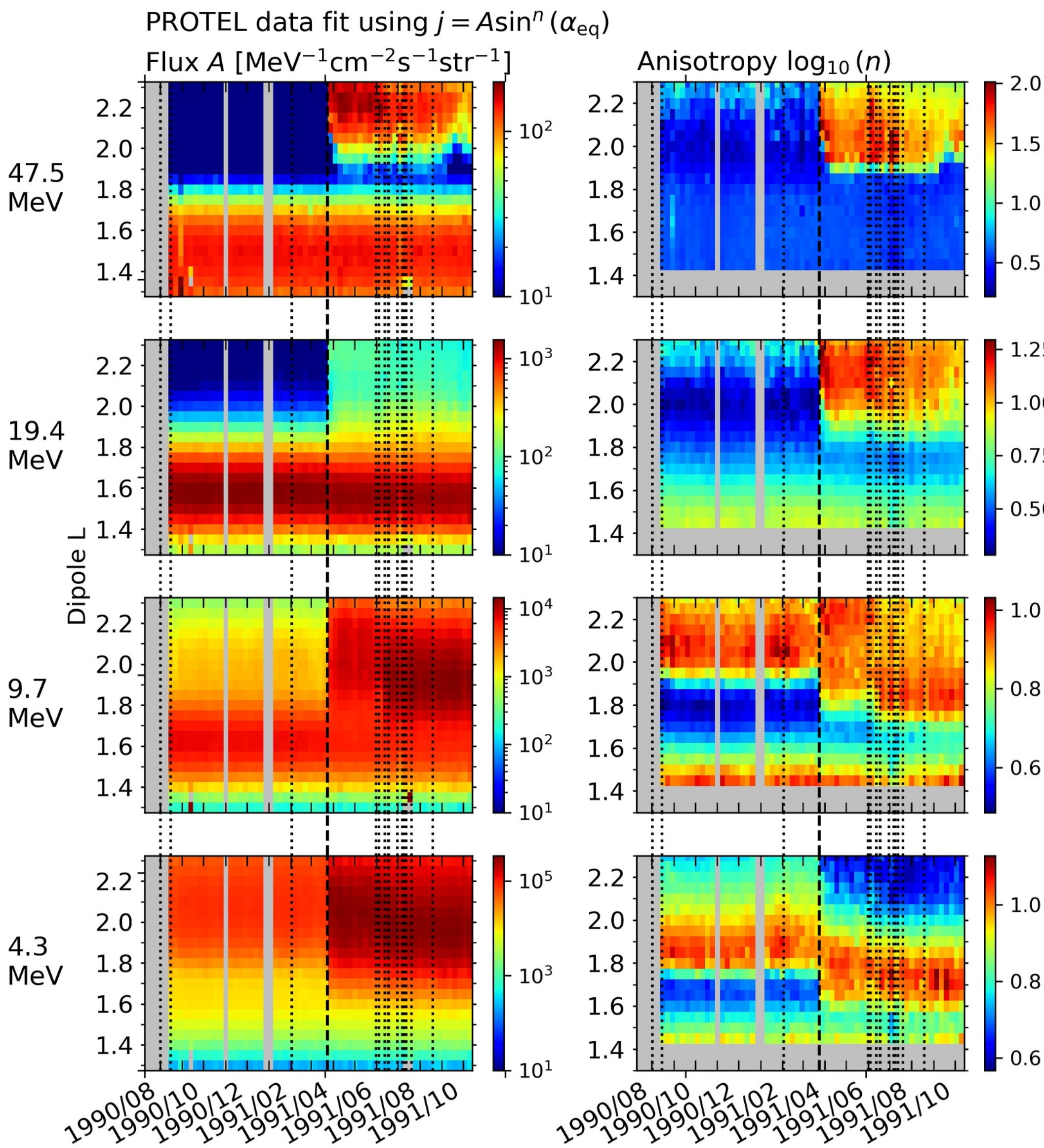

Figure 2. PROTEL data at selected energy channels, showing flux at $\alpha_{eq} = 90°$ (left panels) from the fitted pitch angle distributions given by $j = A\sin^n(\alpha_{eq})$ with ~1 week data average periods, and anisotropy of the pitch angle distributions (right panels) given by $\log_{10}(n)$. Vertical dotted lines indicate magnetic disturbances corresponding to Table 1 of Hudson et al. (1997), with the March 1991 storm shown by a dashed line.

order of magnitude at 1–20 MeV reaching $L < 2$. Figure 2 also demonstrates changes to particle pitch angle distributions following the enhancement, with an increase in anisotropy seen to affect 4.3 MeV protons at $L \approx 1.7$. Inward radial transport of a particle with simultaneous conservation of M results in betatron acceleration, increasing momentum $p_\perp$ relative to $p_\parallel$. The increase in anisotropy shown by Figure 2 is thus an indicator of inward transport.

3. Modeling Particle Redistribution

We hypothesize that the electromagnetic pulse associated with the March 1991 event caused some radiation belt protons to be nonadiabatically redistributed to different drift shells but remain trapped, and that this internal shift explains the increase in flux at 1–20 MeV shown in Figure 2.

To investigate this hypothesis, test protons were traced backwards in time over the March 1991 disturbance period using the Trajectory Redistribution In Phase Space (TRIPS) code, which has been made publicly available (Lozinski & Desai, 2025). This process involved specifying an initial six-dimensional state vector for each particle, then evolving it over small timesteps according to the Lorentz force. TRIPS allows a user to specify the initial state vector in terms of the three adiabatic invariants M (or E), α_{eq_a} and L, together with the gyration, bounce and drift phases ϕ_1, ϕ_2 and ϕ_3 respectively. We made use of this feature to investigate the redistribution of particles to specific drift orbits as follows.

First, we established the set of three-dimensional coordinates

$$P' = \{\boldsymbol{x}'_a | a \in A\} \tag{3}$$

where $\boldsymbol{x}'_a = \left(E'_a, \alpha_{\mathrm{eq}}{}'_a, L'_a\right)$ and A is the index set, and the prime notation indicates an instance in time just after the 24 March 1991 disturbance period ("post-event"). Coordinates in P' form a grid of points in the parameter space $E' \times \alpha'_{\mathrm{eq}} \times L'$ with $\alpha_{\mathrm{eq}}{}' = \{85\,°, 87.5°\}$, $L' = \{1.8, 1.9, 2.0, 2.1\}$ and $E' = \{4.3, \ldots 36.3 \text{ MeV}\}$ to coincide with 13 energy channels of PROTEL. This resulted in $|A| = 104$ unique coordinates, each representing a drift orbit.

For each drift orbit in P', unique combinations of post-event gyration, bounce and drift phase were generated to yield the six parameters $\left(E', \alpha_{\mathrm{eq}}{}', L', \phi'_1, \phi'_2, \phi'_3\right)$, and each set of parameters was then used to initialize a test proton. One hundred fifty particles were initialized per drift orbit using this method. Each particle was traced backwards in time from 24 March 1991 03:44:20 to 03:41:20 UT ($\Delta t = -180$ s), and their resultant "pre-event" state vectors $\left(E, \alpha_{\mathrm{eq}}, L, \phi_1, \phi_2, \phi_3\right)$ were then given by TRIPS. This method of reverse-time tracing revealed how particles were redistributed from various other drift orbits to $\boldsymbol{x}'_a$ during the event. Appendix A presents our full method for tracing particles, analyzing their redistribution, and accounting for potential undersampling by the number of test protons.

Figure 3 plots pre-event L and ϕ_3 of all test particles traced backwards in time from $L' = 2.1$ over the 24 March 1991 disturbance. Groups of particles were initialized from the same M$'$, corresponding to an energy channel on PROTEL, and these groups have been separated in Figure 3 as indicated by white and gray shading, with the vertical axis repeated for each group. Our results showed that the disturbance did not alter the first invariant of any particle significantly, thus M $\approx$ M$'$. However, Figure 3 highlights the spread in pre-event L of particles traced backwards from the same L'.

Figure 3 shows that the March 1991 disturbance enabled the transport of particles from $L = 3.2$ to 2.1 for a narrow range of initial drift phases at M $\approx$ 400 MeV/G. Comparison to the pre-event L distributions at higher or lower M illustrates the dependence of inward transport on drift velocity, with the peak at M $\approx$ 400 MeV/G occurring due to drift resonance. The interaction of a radiation belt particle with an electric field pulse also depends on its initial phase along the drift orbit because the electromagnetic perturbation is asymmetrical around the magnetosphere. In particular, Figure 3 demonstrates that radial transport depends strongly on the initial combination of L and ϕ_3 for a given M.

Finally, the test particle results were used to predict post-event phase space density $f'_a = f'(\boldsymbol{x}'_a)$ at each coordinate in P' using the method presented in Appendix A. This method assumes f'_a to be the result of particles moving to $\boldsymbol{x}'_a$ from a set of other coordinates $\boldsymbol{\mu}_{(a,k)}$ over the disturbance period, with f'_a modeled by

$$f'_a \approx \sum_{k=1}^{K_a} f_{(a,k)}\ \Theta_{(a,k)} \tag{4}$$

where $f_{(a,k)} = f\left(\boldsymbol{\mu}_{(a,k)}\right)$ is a 1-week average of pre-event phase space density measurements from PROTEL and $\Theta_{(a,k)}$ is the estimated fraction of phase space density transferred from $\boldsymbol{\mu}_{(a,k)}$ to $\boldsymbol{x}'_a$. Since Equation 4 only takes into account the rearrangement of a pre-existing trapped population, our hypothesis is evaluated by comparing predictions f'_a to PROTEL measurements made after the event.

10.1029/2025JA033871

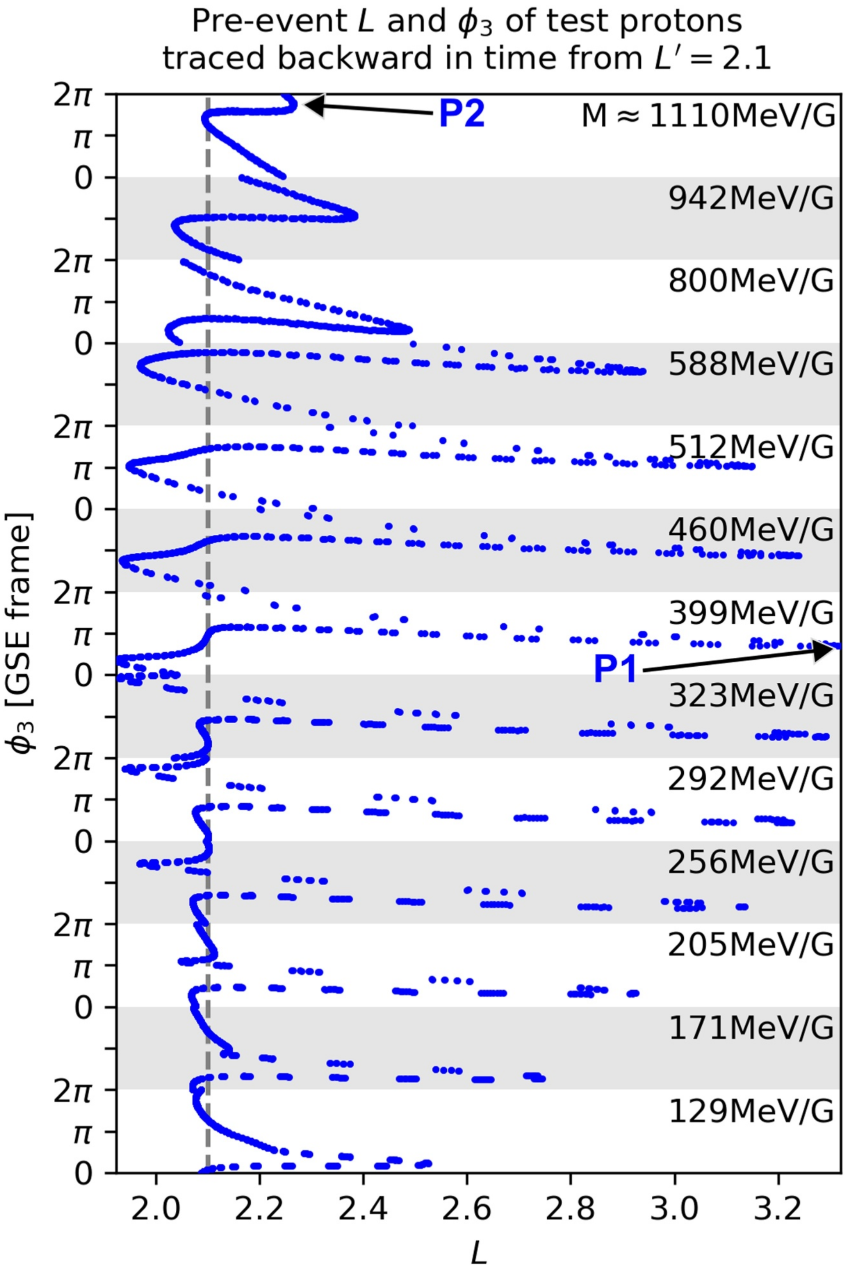

Figure 3. Pre-event distributions of L and ϕ_3 for a selection of test particles. These particles were initialized at $L' = 2.1$ (gray dashed vertical line) with various combinations of gyration, bounce and drift phases. The selection of test particles is split into groups of similar $M \approx M'$ as indicated by white and gray shading, with the vertical axis repeated for each group. Also annotated are specific test protons P1 and P2, whose trajectories are plotted in Figure 5.

4. Results

Figure 4 presents the predicted phase space density f'_a at $\alpha_{eq} = 85°$ (left panel, dotted blue line) and 87.5° (right panel, dotted blue line) alongside PROTEL observations of phase space density made before (solid red line) and after (solid blue line) the 24 March 1991 event.

The error bar around each observation in Figure 4 represents the standard deviation of individual phase space density measurements within each PROTEL pitch angle bin range and time average period. These observations were averaged over ~1 week pre and post-storm time windows, therefore the error bars indicate variation in individual measurements during these time periods. Both figures exhibit the largest error bars in the pre-storm

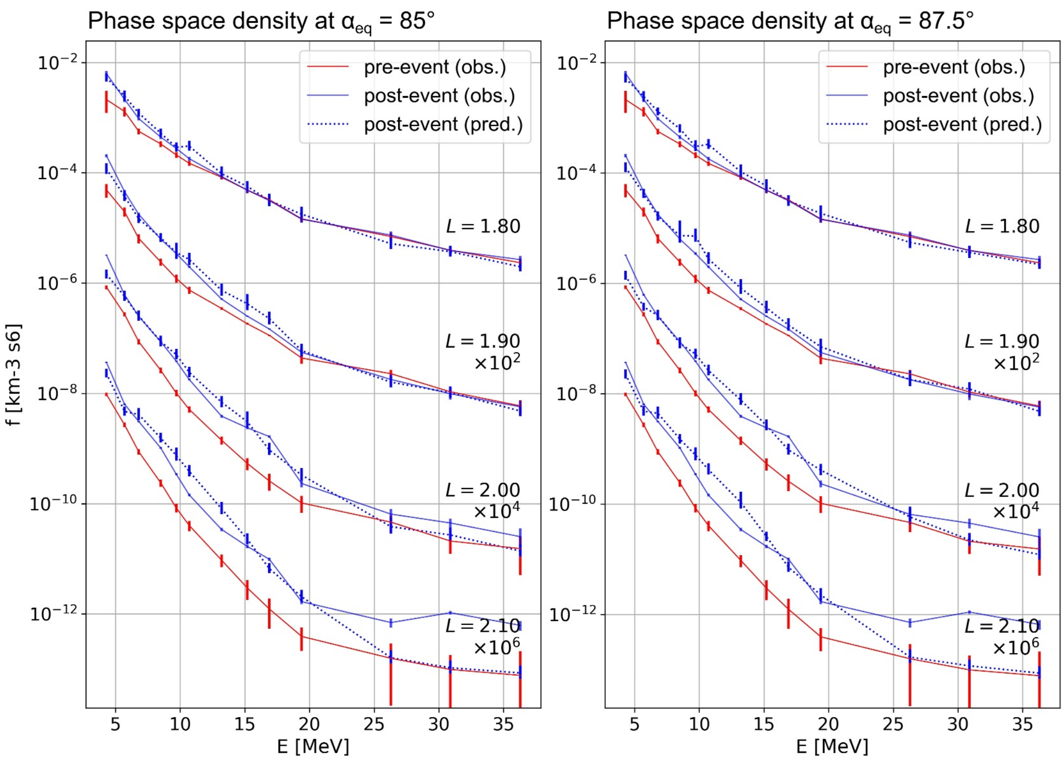

Figure 4. Phase space density at $\alpha_{eq} = 85°$ (left panel) and 87.5° (right panel) following the 24 March 1991 event predicted by modeling the internal redistribution of trapped protons (dotted blue line) versus CRRES PROTEL observations from before (solid red line) and after (solid blue line) the event. Prediction error bars represent uncertainty in the fractions of phase space density transported between various coordinates by the pulse, observation error bars represent variation in flux measurements over time averaging windows and pitch angle bins used to derive the fit in Equation 2.

average period at $L = 2.1$ and >20 MeV, where phase space density is also lowest. This raises the question of whether or not an instrument noise floor was responsible for these error bars. However, Gussenhoven et al. (1993, Figure 2) present radial profiles of measured >20 MeV flux extending smoothly to $L > 2.5$, where flux is even lower, suggesting that the pre-storm error bars at $L = 2.1$ and >20 MeV in Figure 4 are mostly the result of real time variation.

The error bars around each prediction in Figure 4 represent error in the estimates $\Theta_{(a,k)}$ used to represent the fraction of phase space density transported from another coordinate $\boldsymbol{\mu}_{(a,k)}$ to $\boldsymbol{x}'_a$. This error comes from the correction factor $C_{(a,k)}$ introduced in Appendix A, Equation A4, and discussed further in Appendix B. Predictions also depend on pre-event phase space density observations, and the observational error therefore leads to another component of error in the predictions. Since observational error is illustrated separately in Figure 4, this component has been excluded from the prediction error bars.

The difference of only $\Delta\alpha_{eq} = 2.5°$ between the results shown in the left and right panels of Figure 4 leads to them being very similar. The main purpose of including both was to provide a secondary validation of the method for predicting f'_a using Equation 4.

5. Discussion

Figure 4 shows a within factor of two agreement between predicted post-event phase space density f'_a (dotted blue line) and PROTEL measurements (solid blue line) in the energy range 1–20 MeV at all L. This suggests, in support of our hypothesis, that the 1–20 MeV enhancement seen following the 24 March 1991 event can be accounted for by the redistribution of already-trapped protons, which tended to be shifted toward lower L shells by the pulse as demonstrated by the test particles simulation in Figure 3.

Conversely, Figure 4 shows a discrepancy between predictions and measurements at >20 MeV and $L \geq 2$. This suggests that the >20 MeV, $L \geq 2$ distribution cannot be accounted for by the redistribution of already-trapped protons. We investigated further by analyzing the trajectories of individual test particles, and identified two for comparison:

- Proton P1 was identified as the test particle traced backwards in time from $L = 2.1$ that got transported farthest in L. P1 has $\mathrm{M} = 403$ MeV/G and was inwardly transported by $\Delta L \approx 1.22$, resulting in energization from 3.3 to 13.2 MeV;
- Proton P2 was identified as the test particle traced backwards in time from $L = 2.1$ that got transported farthest in L but with the extra condition that its pre-event energy was ≥30 MeV. P2 has $\mathrm{M} = 1111$ MeV/G and was inwardly transported by $\Delta L \approx 0.15$, resulting in energization from 30 to 36.3 MeV.

Particles P1 and P2 are indicated in Figure 3, and their trajectories are plotted in Figure 5 in the X-Y plane of the MAG frame. Each panel of Figure 5 shows P1 and P2 at a snapshot in time, with simulation time labeled in the top left of each panel. The azimuthal component of the electric field is indicated by background color in each panel, showing the arrival of the pulse. Each black dot along the trajectories of P1, P2 is separated by $\Delta t \approx 3.7$ s to illustrate the respective drift velocities. The black lines follow prior locations of each particle's gyrocenter, computed via reanalysis of the Lorentz trajectories. The Earth's surface is represented as a gray circle. Due to inward transport and energization, the drift period of P1 changes from ∼230 to ∼90 s, whilst the drift period of P2 remains at ∼40 s (see Figure B.3, Walt, 1994).

Figure 5 illustrates several stages of particle transport: panel "a" shows P1 arriving at the pulse before P2; panel "b" shows the pulse beginning to reflect off Earth's ionosphere as P2 drifts into it; panel "c" shows the pulse developing a bipolar signature and deflecting around Earth; and panel "d" shows P2 overtaking P1 and the pulse due to its faster drift velocity. Figure 5 thus shows why P1 achieved further inward transport than P2: when P1 arrives at the pulse in panel "a," its drift velocity allows it to skim the arriving wavefront and experience prolonged negative E_ϕ, which accelerates it sharply inwards. On the other hand, P2 has a drift velocity faster than the pulse, and experiences an oscillating E_ϕ as it enters and leaves the pulse region with only modest radial transport. Figure 5, bottom panel, plots the electric field experienced by P1 and P2 along their trajectories to demonstrate this.

One theory to explain the discrepancy between predictions and measurements at >20 MeV in Figure 4 is that some fraction of post-event phase space density originates from a SEP source, and this was not taken into account by Equation 4. However, it was somewhat surprising to find that the test particles traced backwards from these coordinates, such as P2, did not achieve transport from high L. Instead, we found that these particles could not be effectively transported by the pulse because the drift velocity was too high, resulting in only small radial shifts. Therefore, to explain the discrepancy, an SEP source would have to transport particles to $L \approx 2.25$ within the first ∼80 s of the event, in order to undergo even further inward transport along the trajectory of P2.

Our test particle results demonstrate that drift resonance explains the shift of particles inward to $L \sim 2$, and occurs at much lower M compared to examples of particle transport at higher L investigated by previous literature, for example, Figure 3 of Hudson et al. (1996) and Figure 10 of Gannon et al. (2005). This is because at fixed M, energy and drift velocity increase as L decreases. Therefore, resonant interaction with the pulse at low L occurs at lower M. The long timescale for radial diffusion in the enhancement region (Lozinski, Horne, Glauert, Del Zanna, & Claudepierre, 2021) may lead such enhancements to be long-lived, as indicated by CRRES observations in the months following the event.

A potential source of error not included in Figure 4 is the model electromagnetic perturbation used for particle tracing, derived using Equation 1. Figure 1 (top panel) shows that the model causes a bipolar electric field pulse at the location of CRRES, but it is delayed relative to observations. In our simulations, this may have resulted in a delay to the inward transport of test particles, obscuring information about the true magnetic local time of each particle just prior to transport, and shifting the drift phases shown in Figure 3. In addition, Figure 1 shows that the model slightly underestimates the electric field amplitude by ∼2 mV/m, which may cause test particles to undergo less inward transport than in reality. The discrepancy between the model and real pulse may also be different in other regions of the magnetosphere, where there are no CRRES observations to compare with. Several alternative techniques to model an electromagnetic perturbation have been demonstrated in literature, for example,: Hudson et al. (2023) used upstream solar wind parameters measured at L1 to drive global MHD simulations, whilst other

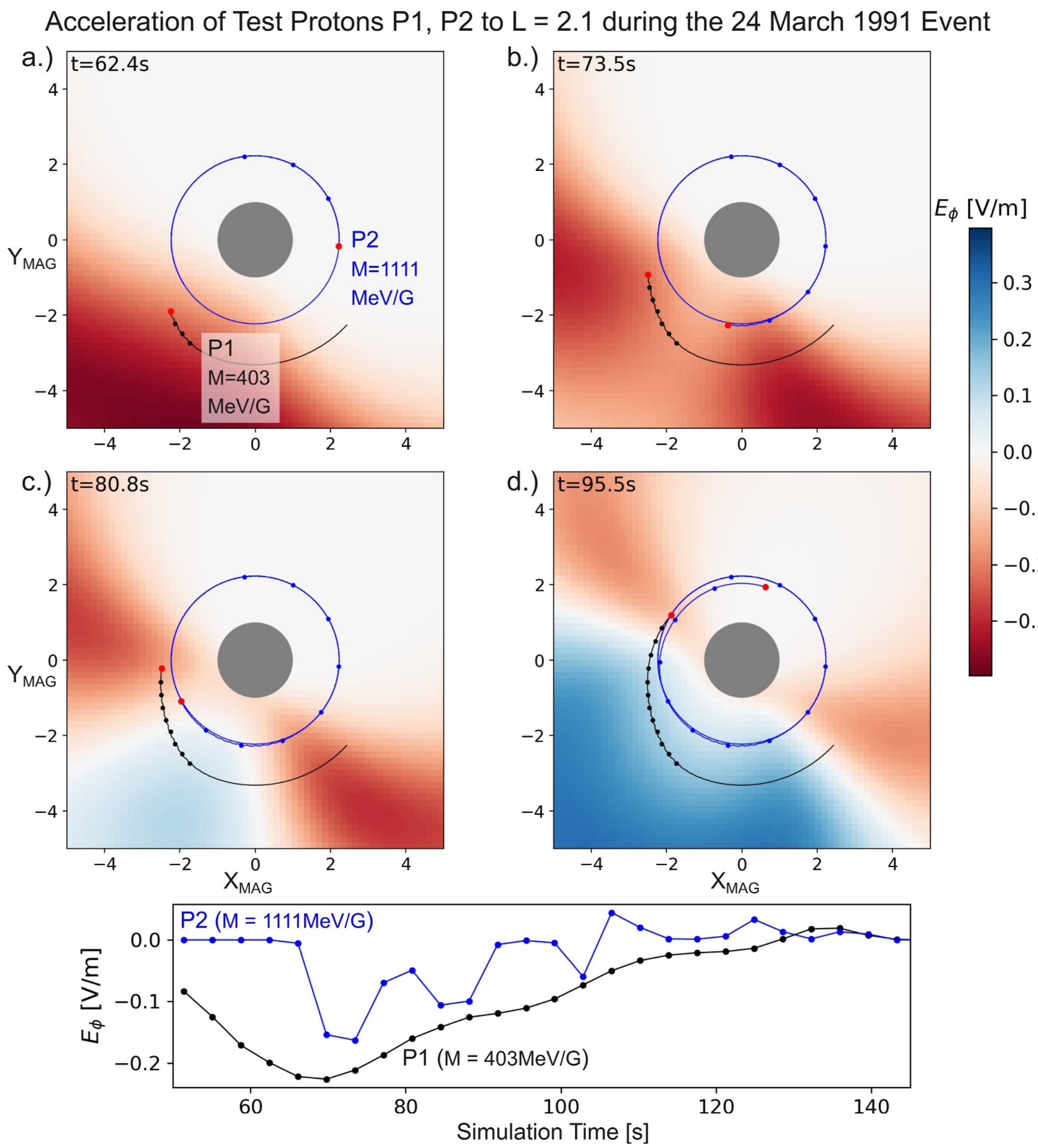

Figure 5. Panels a through d show snapshots of two test protons (P1 and P2) interacting with the electric field pulse in the X-Y plane of the MAG frame during the 24 March 1991 event simulation, with the azimuthal electric field indicated by color. Panels show: (a) P1 arriving at the pulse wavefront and being accelerated inward; (b) P2 arriving at the pulse as it begins to reflect from the ionosphere; (c) the pulse developing a bipolar signature and deflecting around Earth; and (d) P2 overtaking P1 due to its higher drift velocity. Bottom panel shows the azimuthal electric field as a function of time recorded at P1 and P2 positions.

authors have calculated an induced electric field using a time-varying magnetic field model (Engel et al., 2015; Girgis et al., 2021). One challenge of utilizing MHD simulations is extending the inner boundary to low enough L. Another technique is to tweak free parameters in the pulse model of X. Li et al. (1993) as demonstrated by Gannon et al. (2005).

6. Conclusion

In this study, we identified the enhancements seen in CRRES data at 1–20 MeV, $L \sim 2$ following the 24 March 1991 event to be the result of internal redistribution within the proton belt. This was caused by the electromagnetic pulse induced by shock-driven compression of the magnetosphere which has previously been shown to be responsible for the injection and trapping of SEPs. Our simulations showed that trapped protons underwent drift resonance with the pulse at M $\approx$ 400 MeV/G. This value is at lower M than the drift resonance noted in previous literature to explain inward transport of SEPs from regions of cutoff suppression.

Our work highlights the risk to satellites orbiting near $L = 2$ posed by enhancements of this nature, which can lead to periods of higher solar cell nonionizing dose rate or single event effect occurrence. In particular, our results show that such an enhancement does not depend on an SEP event. Furthermore, the impacts of such an enhancement may be prolonged because of the longer timescales for variation in this region compared with at higher L.

To address the risk, we demonstrated a method to predict the change in phase space density in cases where the electromagnetic field can be modeled, and achieved good agreement with CRRES data. Our method is also conducive to real-time application: only one reverse-time simulation of around 150 particles was needed to predict phase space density at each coordinate, resulting in fast execution, and the method provides an estimate of error, allowing the assimilation of phase space density predictions at discrete coordinates into a continuous model distribution.

The successful application of this method highlights opportunities for future work, including investigation into whether other interplanetary shocks drive similar enhancements. Furthermore, if an electromagnetic perturbation can be predicted ahead of shock arrival, and pre-event proton belt phase space density can be determined from a model, our method can also be used to forecast an imminent redistribution in real-time.

Appendix A: Reverse-Time Particle Tracing to Predict Changes in Phase Space Density

This section describes the method used to predict post-event phase space density at the coordinates $P' = \{\boldsymbol{x}'_a | a \in A\}$ described in Section 3, where $\boldsymbol{x}'_a = \left(E'_a, {\alpha_{\mathrm{eq}}}'_a, L'_a\right)$. To begin, a set of six-dimensional coordinates was derived from P':

$$Q' = \left\{\boldsymbol{\zeta}'_{(a,i)} | (a,i) \in (A \times I)\right\} \tag{A1}$$

where $\boldsymbol{\zeta}'_{(a,i)} = \left(\boldsymbol{x}'_a, {\phi_1}'_{(a,i)}, {\phi_2}'_{(a,i)}, {\phi_3}'_{(a,i)}\right)$. Coordinates $\boldsymbol{\zeta}'_{(a,i)}$ were distributed on a regular grid in the parameter space ${\phi_1}' \times {\phi_2}' \times {\phi_3}'$ of each coordinate $\boldsymbol{x}'_a$. In other words, Q' is a set of coordinates exploring many combinations of gyration, bounce and drift phase along each drift orbit in P'. The set Q' was used to initialize a population of test protons with state vectors $\boldsymbol{\zeta}'_{(a,i)}$, and the trajectories were then traced backwards in time over the March 1991 disturbance period from 24 March 1991 03:44:20 to 03:41:20 UT ($\Delta t = -180$s). This reversely distributed each particle to a coordinate $\boldsymbol{\zeta}_{(a,i)} = \left(\boldsymbol{x}_{(a,i)}, \phi_{1(a,i)}, \phi_{2(a,i)}, \phi_{3(a,i)}\right)$, where the absence of prime indicates a "pre-event" quantity, yielding the set of corresponding pre-event coordinates:

$$Q = \left\{\boldsymbol{\zeta}_{(a,i)} | (a,i) \in (A \times I)\right\} \tag{A2}$$

Particle tracing was performed using the Trajectory Redistribution In Phase Space (TRIPS) code, which includes the following capabilities:

- initializing a test particle at a user-specified set of drift orbit coordinates $(E, \alpha_{\mathrm{eq}}, L)$ and associated phases (ϕ_1, ϕ_2, ϕ_3);
- loading a time-varying electromagnetic field stored on a numerical grid;
- solving the full Lorentz trajectory using the Boris algorithm (Birdsall & Langdon, 1991; Desai et al., 2021);
- re-evaluating the adiabatic invariants and associated phases at the end of a test particle simulation; and
- tracing backwards in time.

At the beginning of a simulation, TRIPS converts from a set of invariant coordinates and associated phases to a position-momentum state vector in three-dimensional space. This works by initializing a particle on the magnetic equator, performing a single bounce orbit with the electromagnetic field frozen, then re-initializing the particle over the specified fraction of the bounce. A similar method is used in reverse to determine bounce phase at the end of a simulation. The electromagnetic field at the particle position was interpolated from the numerical grid described in Section 2.1.

Using the particle tracing results, the following steps were then followed to predict post-event phase space density $f'_a = f'(\boldsymbol{x}'_a)$ for a given post-event coordinate index a:

1. Pre-event coordinates $\boldsymbol{\zeta}_{(a,i)} = \left(\boldsymbol{x}_{(a,i)}, \phi_{1(a,i)}, \phi_{2(a,i)}, \phi_{3(a,i)}\right)$ were extracted from Q, corresponding to $|I|$ test particles that got redistributed from $\boldsymbol{x}_{(a,i)}$ to $\boldsymbol{x}'_a$.
2. Unsupervised clustering was performed on the set of features $\left(1.4\left[L_{(a,i)} - 1\right], \cos\phi_{3(a,i)}, \sin\phi_{3(a,i)}\right)$ to generate clusters $S_{(a,k)}$, where $k = \{1, \dots K_a\}$. The index set of test particles belonging to cluster (a,k) is hereby denoted $\{(a,i) : \pi(i) = k\}$.
   As a result of these two steps, test particles within any given cluster were:
   - transported to the same post-event coordinate $\boldsymbol{x}'_a$, and
   - proximate in their pre-event L and ϕ_3.
     The factor of 1.4 was introduced to weigh the importance of L during clustering, and was determined experimentally to produce good results. This process organized the test particles by their interaction with the pulse, such that particles in a given cluster underwent somewhat uniform transport.
3. A centroid coordinate was calculated for each cluster in three-dimensional phase space:

$$\boldsymbol{\mu}_{(a,k)} = \frac{1}{|S_{(a,k)}|} \sum_{\{(a,i):\pi(i)=k\}} \boldsymbol{x}_{(a,i)} \tag{A3}$$

   Since $|S_{(a,k)}| \ll |I|$, each $\boldsymbol{\mu}_{(a,k)}$ can be considered a representative drift orbit, thus simplifying the overall redistribution: test particles with indices $\{(a,i) : \pi(i) = k\}$ were redistributed from $\sim\boldsymbol{\mu}_{(a,k)}$ to $\boldsymbol{x}'_a$.
   To illustrate this, Figure A1 (left panel) plots a set of pre-event test particle coordinates (dots) and their clustering into six centroids $\boldsymbol{\mu}_{(a,k)}$ (open circles) indicated by color groups, with the post-event coordinate $\boldsymbol{x}'_a$ also shown (black plus). For a given cluster (a,k), consider the realistic pre-event distribution of protons within a small volume of three-dimensional phase space centered at $\boldsymbol{\mu}_{(a,k)}$. If this distribution were evolved forward in time over the March 1991 disturbance, our test particle simulations indicate that some particles would be transported to within a similarly sized volume at $\boldsymbol{x}'_a$. However, many particles would be scattered elsewhere. From this experiment, it would be possible to count the fraction of particles originally at $\boldsymbol{\mu}_{(a,k)}$ that got redistributed to $\boldsymbol{x}'_a$. We hereby refer to this fraction as $\Theta_{(a,k)}$.
   One can assume a realistic distribution to be uniformly distributed in gyration, bounce and drift phase. In contrast, the pre-event coordinates of each test particle at $\boldsymbol{\mu}_{(a,k)}$ tended to occupy a coherent fraction of $\phi_1 \times \phi_2 \times \phi_3$ space. To illustrate this, Figure A1 (right panels) plots $\left\{\left(\phi_{2(a,i)}, \phi_{3(a,i)}\right) : \pi(i) = k\right\}$ for $k = 2, 4$ and 6 (black dots).
   We therefore estimated the fraction of particles $\Theta_{(a,k)}$ transported from $\boldsymbol{\mu}_{(a,k)}$ to $\boldsymbol{x}'_a$ in a realistic distribution as the fraction of $\phi_1 \times \phi_2 \times \phi_3$ space occupied by the test particles traced backwards to $\boldsymbol{\mu}_{(a,k)}$. This can be taken as the volume of the convex hull of points in $\phi_1 \times \phi_2 \times \phi_3$ space multiplied by a correction factor $C_{(a,k)}$ to account for undersampling:

$$\Theta_{(a,k)} = C_{(a,k)}\ \mathrm{Vol}\left(\mathrm{Hull}\left(\left\{\boldsymbol{\phi}_{(a,i)} : \pi(i) = k\right\}\right)\right) \tag{A4}$$

   To illustrate this, Figure A1 (right panels) plots three example hulls in $\phi_2 \times \phi_3$ space (red lines). The correction factor and its associated error is discussed and numerically derived in Appendix B.
4. The post-event phase space density $f'_a = f'(\boldsymbol{x}'_a)$ was then estimated as the weighted average of pre-event phase space densities given by $f'_a \approx \sum_{k=1}^{K_a} f_{(a,k)}\ \Theta_{(a,k)}$ (Equation 4), where $f_{(a,k)} = f\left(\boldsymbol{\mu}_{(a,k)}\right)$ was interpolated from PROTEL measurements in the pre-storm average window.

The above method was applied using the scikit-learn agglomerative clustering algorithm in step 2 with a fixed linkage distance threshold value of $d = 2.4$ (Pedregosa et al., 2011). This controlled the number of clusters K_a, generally between two and six depending on the coordinate range spanned by the set of $\boldsymbol{\zeta}_{(a,i)}$. As d (K_a) is decreased (increased), each $\Theta_{(a,k)}$ decreases because the volume of $\phi_1 \times \phi_2 \times \phi_3$ space

10.1029/2025JA033871

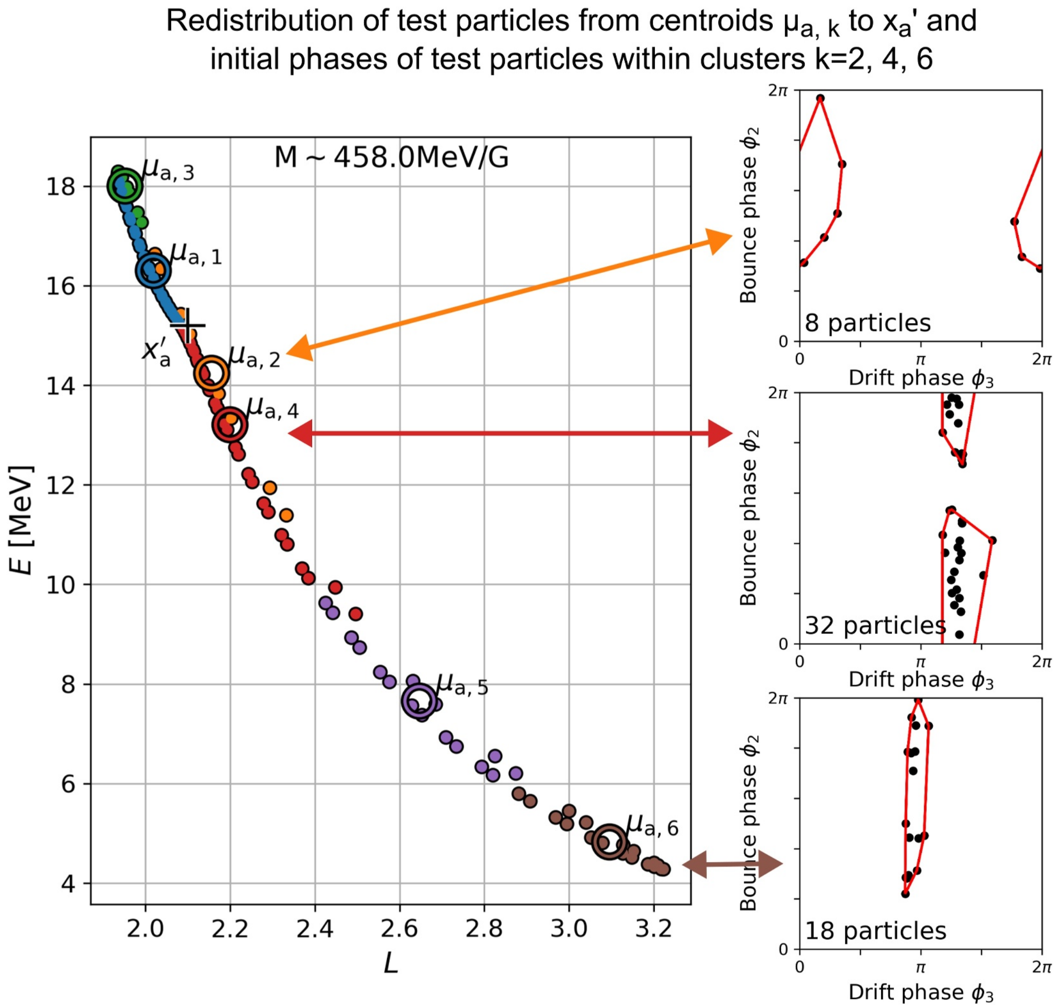

Figure A1. Pre-event E, L (colored dots) of test particles (a, i), traced backwards in time from $\boldsymbol{x}_a'$ (black cross). Test particles were clustered based on their pre-event features $\left(1.4\left[L_{(a,i)} - 1\right], \cos\phi_{3(a,i)}, \sin\phi_{3(a,i)}\right)$, and the color of each dot indicates the cluster that the test particle belongs to. Panels on the right plot the pre-event phases ϕ_2 *and* ϕ_3 of test particles (black dots), which are separated into different plots based on their cluster, and the convex hull (red lines) drawn around each set of phase coordinates.

spanned by particles within a given cluster reduces. Therefore Equation 4 is not overly sensitive to K_a, and varies only due to the efficiency of clustering and test particle sampling.

Appendix B: Estimating a Sampled Volume Using the Convex Hull

The method in Appendix A relies on determining a volume of $\phi_1 \times \phi_2 \times \phi_3$ space with unknown bounds based on a distribution of test particles occupying the volume. An estimate was derived by approximating the bounds by a convex hull encompassing the test particle coordinates, but this calculation is sensitive to undersampling as the test particles may not be spread throughout the whole volume. To demonstrate, consider a number of points randomly distributed inside a sphere: if a convex hull is drawn around these points, its volume will approximate the volume of the bounding sphere to some extent. We investigated this by generating sets of random spherical coordinates (r, θ, ϕ) inside a sphere with unit radius like so:

$$r = V^{1/3} \tag{B1}$$

$$\theta = \cos^{-1} A \tag{B2}$$

$$\phi \sim U[0, 2\pi] \tag{B3}$$

where $V \sim U[0,1]$, $A \sim U[-1,1]$ and U is a uniform distribution. Figure B1, third panel, plots the volume of a convex hull drawn around the collection of points, divided by the volume of the sphere, versus the number of points randomly generated inside the sphere. The experiment is repeated 100 times for each number of sample points, and the standard deviation of results is indicated by the shaded blue region. Figure B1 shows that the convex hull volume is always an underestimate but becomes a better approximation as the number of points increases.

The same experiment is repeated in two dimensions in the second panel of Figure B1 by projecting the set of points onto a 2D surface, and repeated in one dimension in the first panel by projecting the set of points onto a line. Figure B1 (right subplot) illustrates a two dimensional example using 61 sample points: the blue circle represents the volume in which the points are generated, also projected into two dimensions, and the red line is the convex hull. The ratio plotted is the area of the red convex hull divided by the area of the blue circle.

Figure B1 demonstrates that the ratio by which the convex hull underestimates the volume can be determined based on the number of sample points. Therefore, even if a volume is under-sampled (i.e., only ~10 points inside it are known), its size can be estimated by dividing the convex hull volume by this ratio. We applied this technique by interpolating the ratio plotted on the vertical axis for the number of sample coordinates in a given cluster. The correction factor $C_{(a,k)}$ was then calculated as the inverse of this ratio, and the standard deviation was used to derive an associated error.

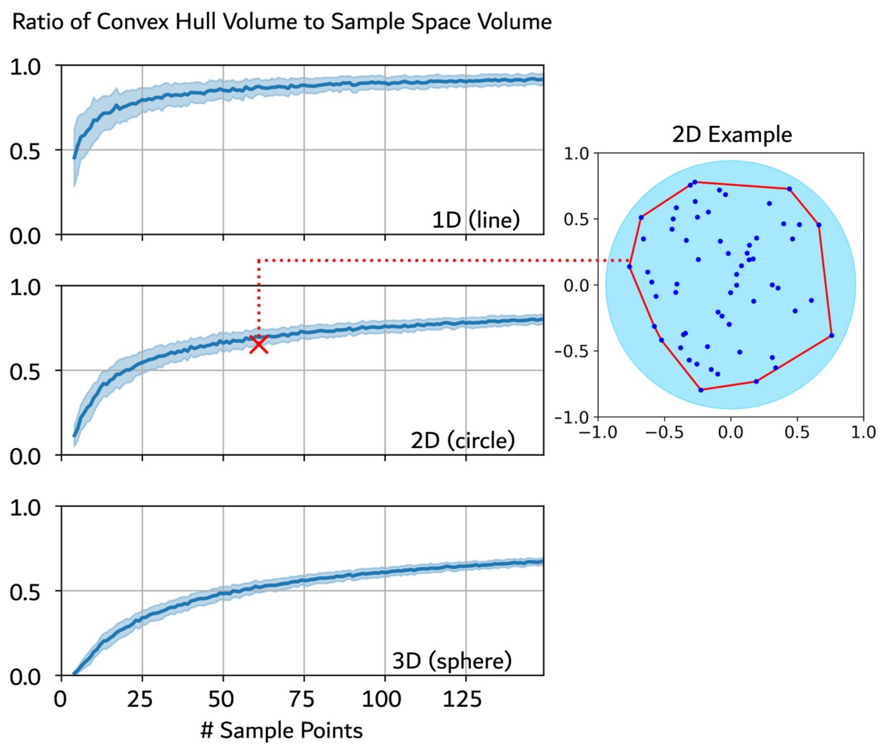

Figure B1. The volume of a convex hull drawn around a collection of points divided by the volume of the spheroid in which the points are randomly distributed, versus the number of points distributed. Panels top to bottom show the same experiment within a one, two and three-dimensional volume, and the right panel shows an example convex hull (red line) drawn around the points (blue dots) in two dimensions, with the bounding area in blue. The standard deviation (blue shading surrounding each plot) is derived from repeating each experiment 100 times.

Data Availability Statement

The Combined Release and Radiation Effects Satellite (CRRES) Fluxgate Magnetometer measurements (H. J. Singer & Mullen, 2010) were retrieved from the Virtual Magnetospheric Observatory (VMO) hosted by IGPP/UCLA at https://vmo.igpp.ucla.edu/data1/CRRES/MAG/PT30S/. The CRRES Langmuir Probe instrument measurements (Mozer & Mullen, 2025) were retrieved from the Virtual Magnetospheric Observatory (VMO) hosted by IGPP/UCLA at http://vmo.igpp.ucla.edu/data1/CRRES/LPI/PT30S/. CRRES PROTEL data (Mullen & Brautigam, 2021) were retrieved from the NASA Space Physics Data Facility at https://spdf.gsfc.nasa.gov/pub/data/crres/particle_protel/. The Trajectory Redistribution In Phase Space code (Lozinski & Desai, 2025) used for particle tracing simulations can be accessed at https://github.com/atmosalex/pt.git or https://doi.org/10.5281/zenodo.14908242. Authors acknowledge the use of the IRBEM library, the latest version of which can be found at https://doi.org/10.5281/zenodo.6867552.

Acknowledgments

Alexander Lozinski and Adam Kellerman acknowledge support from NASA Grant 80NSSC23K0096 and NSF Grant 2149782. Jacob Bortnik acknowledges support from subgrant 1559841 to the University of California, Los Angeles, from the University of Colorado Boulder under NASA Prime Grant agreement no. 80NSSC20K1580. Richard B. Horne and Sarah A. Glauert were supported by Natural Environment Research Council (NERC) Grant NE/V00249X/1 (Sat-Risk) and NE/Y006178/1 (PRESCIENT). Ravindra T. Desai acknowledges an STFC Ernest Rutherford Fellowship ST/W004801/1, and NERC Grants NE/P017347/1 and NE/V003062/1.

References

Albert, J. M., Ginet, G. P., & Gussenhoven, M. S. (1998). Crres observations of radiation belt protons: 1. Data overview and steady state radial diffusion. *Journal of Geophysical Research*, *103*(A5), 9261–9273. https://doi.org/10.1029/97JA02869

Birdsall, C. K., & Langdon, A. B. (1991). *Plasma physics via computer simulation*. CRC Press. https://doi.org/10.1201/9781315275048

Blake, J. B., Kolasinski, W. A., Fillius, R. W., & Mullen, E. G. (1992). Injection of electrons and protons with energies of tens of MeV into L < 3 on 24 march 1991. *Geophysical Research Letters*, *19*(8), 821–824. https://doi.org/10.1029/92GL00624

Daglis, I. A., Thorne, R. M., Baumjohann, W., & Orsini, S. (1999). The terrestrial ring current: Origin, formation, and decay. *Reviews of Geophysics*, *37*(4), 407–438. https://doi.org/10.1029/1999RG900009

Desai, R. T., Eastwood, J. P., Horne, R. B., Allison, H. J., Allanson, O., Watt, C. E. J., et al. (2021). Drift orbit bifurcations and cross-field transport in the outer radiation belt: Global MHD and integrated test-particle simulations. *Journal of Geophysical Research: Space Physics*, *126*(10), e2021JA029802. https://doi.org/10.1029/2021JA029802

Engel, M. A., Kress, B. T., Hudson, M. K., & Selesnick, R. S. (2015). Simulations of inner radiation belt proton loss during geomagnetic storms. *Journal of Geophysical Research: Space Physics*, *120*(11), 9323–9333. https://doi.org/10.1002/2015JA021568

Gannon, J., Li, X., & Temerin, M. (2005). Parametric study of shock-induced transport and energization of relativistic electrons in the magnetosphere. *Journal of Geophysical Research*, *110*(A12), A12206. https://doi.org/10.1029/2004ja010679

Girgis, K. M., Hada, T., Matsukiyo, S., & Yoshikawa, A. (2021). Inner radiation belt simulations of the proton flux response in the south Atlantic anomaly during the geomagnetic storm of 15 may 2005. *Journal of Space Weather and Space Climate*, *11*, 48. https://doi.org/10.1051/swsc/2021031

Gussenhoven, M., Mullen, E., Violet, M., Hein, C., Bass, J., & Madden, D. (1993). Crres high energy proton flux maps. *IEEE Transactions on Nuclear Science*, *40*(6), 1450–1457. https://doi.org/10.1109/23.273519

Horne, R. B., & Pitchford, D. (2015). Space weather concerns for all-electric propulsion satellites. *Space Weather*, *13*(8), 430–433. https://doi.org/10.1002/2015SW001198

Hudson, M. K., Elkington, S. R., Lyon, J. G., Marchenko, V. A., Roth, I., Temerin, M., et al. (1997). Simulations of radiation belt formation during storm sudden commencements. *Journal of Geophysical Research*, *102*(A7), 14087–14102. https://doi.org/10.1029/97JA03995

Hudson, M. K., Elkington, S. R., Lyon, J. G., Marchenko, V. A., Roth, I., Temerin, M., & Gussenhoven, M. S. (1996). MHD/particle simulations of radiation belt formation during a storm sudden commencement. In *Radiation belts: Models and standards* (pp. 57–62). American Geophysical Union (AGU). https://doi.org/10.1029/GM097p0057

Hudson, M. K., Engel, M. A., Kress, B. T., Li, Z., Patel, M., & Selesnick, R. S. (2023). Simulated trapping of solar energetic protons for the 8–10 March 2012 geomagnetic storm: Impact on inner zone protons as measured by van Allen probes. *Journal of Geophysical Research: Space Physics*, *128*(2), e2022JA031106. https://doi.org/10.1029/2022JA031106

Jenkins, P. P., Bentz, D. C., Barnds, J., Binz, C. R., Messenger, S. R., Warner, J. H., et al. (2014). Tacsat-4 solar cell experiment: Two years in orbit. In *10th European space power conference, Noordwijkerhout, Netherlands* (Vol. 14).

Kress, B. T., Hudson, M. K., Perry, K. L., & Slocum, P. L. (2004). Dynamic modeling of geomagnetic cutoff for the 23–24 November 2001 solar energetic particle event. *Geophysical Research Letters*, *31*(4), L04808. https://doi.org/10.1029/2003GL018599

Kress, B. T., Hudson, M. K., & Slocum, P. L. (2005). Impulsive solar energetic ion trapping in the magnetosphere during geomagnetic storms. *Geophysical Research Letters*, *32*(6), L06108. https://doi.org/10.1029/2005GL022373

Kress, B. T., Rodriguez, J. V., Boudouridis, A., Onsager, T. G., Dichter, B. K., Galica, G. E., & Tsui, S. (2021). Observations from NOAA'$_S$ newest solar proton sensor. *Space Weather*, *19*(12), e2021SW002750. https://doi.org/10.1029/2021SW002750

Li, X., Roth, I., Temerin, M., Wygant, J., Hudson, M., & Blake, J. (1993). Simulation of the prompt energization and transport of radiation belt particles during the march 24, 1991 ssc. *Geophysical Research Letters*, *20*(22), 2423–2426. https://doi.org/10.1029/93gl02701

Li, X., Selesnick, R., Schiller, Q., Zhang, K., Zhao, H., Baker, D. N., & Temerin, M. A. (2017). Measurement of electrons from albedo neutron decay and neutron density in near-earth space. *Nature*, *552*(7685), 382–385. https://doi.org/10.1038/nature24642

Li, Z., Engel, M., Hudson, M., Kress, B., Patel, M., Qin, M., & Selesnick, R. (2021). Solar energetic proton access to the inner magnetosphere during the september 7–8, 2017 event. *Journal of Geophysical Research: Space Physics*, *126*(7), e2021JA029107. https://doi.org/10.1029/2021JA029107

Lozinski, A. R., & Desai, R. T. (2025). Trajectory redistribution in phase space python code [Software]. *Zenodo*. https://doi.org/10.5281/zenodo.14908242

Lozinski, A. R., Horne, R. B., Glauert, S. A., Del Zanna, G., & Albert, J. M. (2021). Optimization of radial diffusion coefficients for the proton radiation belt during the CRRES era. *Journal of Geophysical Research: Space Physics*, *126*(3), e2020JA028486. https://doi.org/10.1029/2020JA028486

Lozinski, A. R., Horne, R. B., Glauert, S. A., Del Zanna, G., & Claudepierre, S. G. (2021). Modeling inner proton belt variability at energies 1 to 10 mev using bas-pro. *Journal of Geophysical Research: Space Physics*, *126*(12), e2021JA029777. https://doi.org/10.1029/2021JA029777

Lozinski, A. R., Horne, R. B., Glauert, S. A., Del Zanna, G., Heynderickx, D., & Evans, H. D. R. (2019). Solar cell degradation due to proton belt enhancements during electric orbit raising to geo. *Space Weather*, *17*(7), 1059–1072. https://doi.org/10.1029/2019SW002213

Lozinski, A. R., Horne, R. B., Glauert, S. A., Kellerman, A. C., Bortnik, J., Claudpierre, S. G., et al. (2024). Modeling field line curvature scattering loss of 1–10 mev protons during geomagnetic storms. *Journal of Geophysical Research: Space Physics*, *129*(4), e2023JA032377. https://doi.org/10.1029/2023ja032377

Mäkelä, P., Gopalswamy, N., Akiyama, S., Xie, H., & Yashiro, S. (2011). Energetic storm particle events in coronal mass ejection–driven shocks. *Journal of Geophysical Research*, *116*(A8), A08101. https://doi.org/10.1029/2011JA016683

Miyake, W., Miyoshi, Y., & Matsuoka, A. (2014). On the spatial extent of the proton radiation belt from solar cell output variation of the akebono satellite. *Advances in Space Research*, *53*(11), 1603–1609. https://doi.org/10.1016/j.asr.2014.03.002

Mozer, F. S., & Mullen, E. G. (2025). Crres electric field and convection drift data [Dataset]. *HPDE*. Retrieved from https://hpde.io/NASA/NumericalData/CRRES/LPI/PT30S.html

Mullen, E. G., & Brautigam, D. (2021). Crres protel 1-min proton distribution functions [Dataset]. *HPDE*. Retrieved from https://hpde.io/NASA/NumericalData/CRRES/PROTEL/PT1M.html

Pedregosa, F., Varoquaux, G., Gramfort, A., Michel, V., Thirion, B., Grisel, O., et al. (2011). Scikit-learn: Machine learning in Python. *Journal of Machine Learning Research*, *12*, 2825–2830.

Pierrard, V., Winant, A., Botek, E., & Péters de Bonhome, M. (2024). The mother's day solar storm of 11 may 2024 and its effect on earth's radiation belts. *Universe*, *10*(10). https://doi.org/10.3390/universe10100391

Reames, D. V. (2001). Seps: Space weather hazard in interplanetary space. In *Space weather* (pp. 101–107). American Geophysical Union (AGU). https://doi.org/10.1029/GM125p0101

Rodbell, K. P. (2020). Low-energy protons—Where and why "rare events" matter. *IEEE Transactions on Nuclear Science*, *67*(7), 1204–1215. https://doi.org/10.1109/TNS.2020.2986642

Selesnick, R. S., & Looper, M. D. (2023). Field-line curvature scattering at the outer boundary of the proton radiation belt. *Journal of Geophysical Research: Space Physics*, *128*(7), e2023JA031509. https://doi.org/10.1029/2023JA031509

Selesnick, R. S., Looper, M. D., & Mewaldt, R. A. (2007). A theoretical model of the inner proton radiation belt. *Space Weather*, *5*(4), S04003. https://doi.org/10.1029/2006SW000275

Sergeev, V., & Tsyganenko, N. (1982). Energetic particle losses and trapping boundaries as deduced from calculations with a realistic magnetic field model. *Planetary and Space Science*, *30*(10), 999–1006. https://doi.org/10.1016/0032-0633(82)90149-0

Singer, H. J., & Mullen, E. G. (2010). Crres 30s magnetic field data [Dataset]. *HPDE*. Retrieved from https://hpde.io/Deprecated/VMO/NumericalData/CRRES/MAG/PT30S.html

Singer, S. F. (1958). Trapped albedo theory of the radiation belt. *Physical Review Letters*, *1*(5), 181–183. https://doi.org/10.1103/physrevlett.1.181

Tsyganenko, N. (1989). A magnetospheric magnetic field model with a warped tail current sheet. *Planetary and Space Science*, *37*(1), 5–20. https://doi.org/10.1016/0032-0633(89)90066-4

Violet, M., Lynch, K., Redus, R., Riehl, K., Boughan, E., & Hein, C. (1993). Proton telescope (PROTEL) on the CRRES spacecraft. *IEEE Transactions on Nuclear Science*, *40*(2), 242–245. https://doi.org/10.1109/23.212348

Walt, M. (1994). *Introduction to geomagnetically trapped radiation*. Cambridge University Press. Retrieved from. https://doi.org/10.1017/cbo9780511524981

Williams, D. J. (1987). Ring current and radiation belts. *Reviews of Geophysics*, *25*(3), 570–578. https://doi.org/10.1029/RG025i003p00570